

## Decoration of growth sector boundaries with nitrogen vacancy centers in as-grown single crystal high-pressure high-temperature synthetic diamond

P. L. Diggle <sup>1,2</sup>, U. F. S. D’Haenens-Johansson,<sup>3</sup> B. L. Green <sup>1</sup>, C. M. Welbourn,<sup>1</sup> Thu Nhi Tran Thi <sup>4</sup>, A. Katrusha <sup>5</sup>,  
W. Wang <sup>3</sup> and M. E. Newton <sup>1,2,\*</sup>


<sup>1</sup>*Department of Physics, University of Warwick, Coventry, CV4 7AL, United Kingdom*

<sup>2</sup>*EPSRC Centre for Doctoral Training in Diamond Science and Technology, United Kingdom*

<sup>3</sup>*Gemological Institute of America, New York City, New York, USA*

<sup>4</sup>*European Synchrotron Radiation Facility (ESRF), Grenoble, France*

<sup>5</sup>*New Diamond Technology Ltd, St. Petersburg, Russia*

 (Received 7 March 2020; revised 23 July 2020; accepted 27 August 2020; published 30 September 2020)

Large ( $>100\text{ mm}^3$ ), relatively pure (type II) and low birefringence single crystal diamond can be produced by high pressure high temperature (HPHT) synthesis. In this study we examine a HPHT sample of good crystalline perfection, containing less than 1 ppb (part per billion carbon atoms) of boron impurity atoms in the  $\{001\}$  growth sector and only tens of ppb of nitrogen impurity atoms. It is shown that the boundaries between  $\{111\}$  and  $\{113\}$  growth sectors are decorated by negatively charged nitrogen vacancy centers ( $\text{NV}^-$ ): no decoration is observed at any other type of growth sector interface. This decoration can be used to calculate the relative  $\{111\}$  and  $\{113\}$  growth rates. The bulk  $\{001\}$  sector contains concentrations of luminescent point defects (excited with 488- and 532-nm wavelengths) below  $10^{11}\text{ cm}^{-3}$  ( $10^{-3}$  ppb). We observe the negatively charged silicon-vacancy ( $\text{SiV}^-$ ) defect in the bulk  $\{111\}$  sectors along with a zero phonon line emission associated with a nickel defect at 884 nm (1.40 eV). No preferential orientation is seen for either  $\text{NV}^-$  or  $\text{SiV}^-$  defects, but the nickel related defect is oriented with its trigonal axis along the  $\langle 111 \rangle$  sector growth direction. Since the  $\text{NV}^-$  defect is expected to readily reorientate at HPHT diamond growth temperatures, no preferential orientation is expected for this defect but the lack of preferential orientation of  $\text{SiV}^-$  in  $\{111\}$  sectors is not explained.

DOI: [10.1103/PhysRevMaterials.4.093402](https://doi.org/10.1103/PhysRevMaterials.4.093402)

### I. INTRODUCTION

Two methods are routinely employed for the synthesis of single crystal diamond: high pressure, high temperature (HPHT) synthesis, and chemical vapor deposition (CVD). Single crystal HPHT diamonds are grown on a small seed crystal using the temperature gradient method in the diamond thermodynamic stability region. Typical solvents are alloys of iron, nickel, and cobalt. Nitrogen has a high solubility in HPHT grown diamond, and can act to change the morphology and/or growth rate of the diamond crystal [1,2]. Nitrogen incorporation can be reduced by the addition of a nitrogen “getter” to the metal solvent, typically titanium, aluminum, or zirconium, which acts to form a stable insoluble complex with nitrogen [3]. In low nitrogen HPHT diamond, boron is often the dominant impurity due to it being present in the carbon source, the solvent/catalyst [4] or even the HPHT capsule materials.

Bulk crystals grow outwards in discrete directions defined by the vector normal to the growth faces involved, culminating in regions known as growth sectors, as shown schematically in Fig. 1. The resulting crystal will usually exhibit only those growth faces that have lower growth velocities. Growth sectors are separated by “growth-sector” boundaries and are

internal surfaces over which the edges between neighboring growth faces have swept during growth. In sections cut from a crystal the boundaries may appear as straight, curved or zig-zag lines with the local direction depending on the instantaneous relative growth velocity of the neighboring faces. It is well understood that the morphology of the HPHT diamond is largely governed by the relative development of  $\{001\}$  and  $\{111\}$  sectors as controlled by the temperature and pressure [5] but also the presence of impurities. The  $\{011\}$ ,  $\{113\}$ , and  $\{115\}$  sectors are often present when the crystal is grown with nitrogen getters to produce type IIa (nitrogen impurities typically less than  $\sim 1$  ppm) diamond [3], and are also seen with the addition of boron to the source material for the production of type IIb (neutral boron impurities detectable by Fourier transform infrared absorption) diamond [6]. The uptake of impurities is growth-sector dependent, as summarized by the modified Kanda diagram [7].

In CVD synthesis, the thermal dissociation of a carbon-containing gas and hydrogen, followed by carbon deposition, yields epitaxial growth of a diamond crystal at below atmospheric pressure [8]. For CVD growth, the chemical purity of the synthesis environment can be controlled with the precision of a semiconductor growth process and hence this approach has undergone a vast research effort in recent years. CVD grown diamond now facilitates a whole host of applications ranging from optical and radiation windows [9–11] to quantum technologies [12,13]. However, keeping

\*Corresponding author: [m.e.newton@warwick.ac.uk](mailto:m.e.newton@warwick.ac.uk)



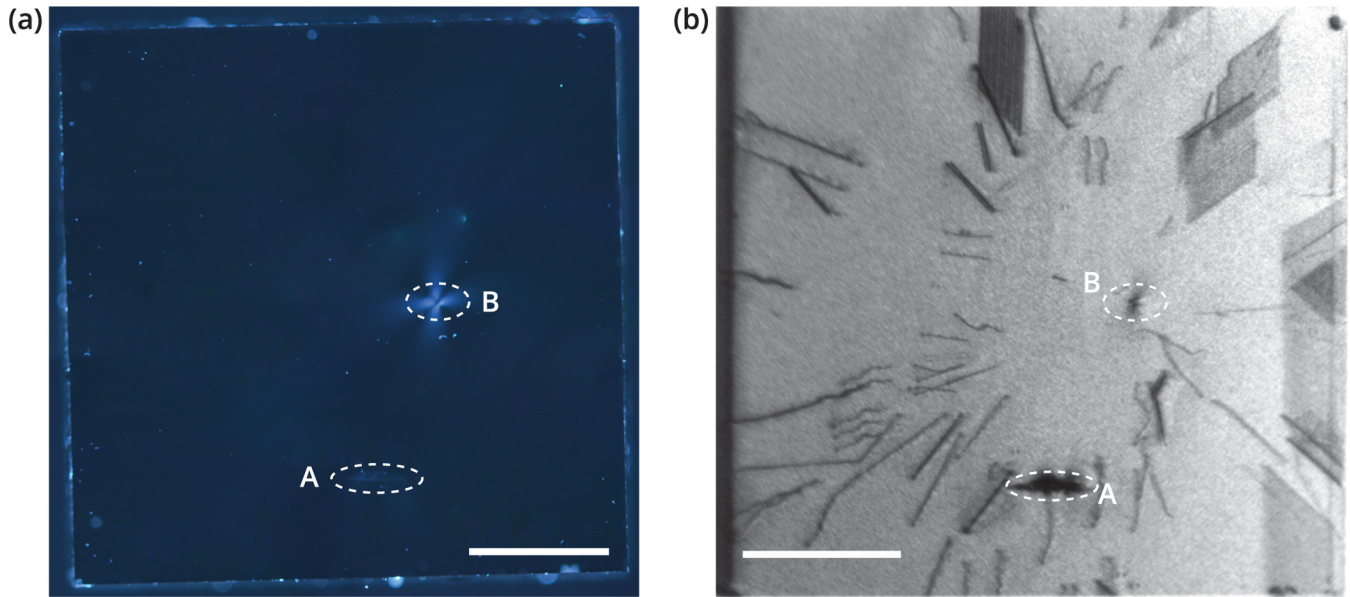


FIG. 2. (a) Cross polarization image of the NDT HPHT sample (polarizers vertical and horizontal) showing a small fracture in the crystal (A) and an inclusion (B). (b) White beam x-ray topograph (400 reflection) with the fracture and inclusion highlighted. (Scale bar: 1 mm).

For low temperature cathodoluminescence (CL) imaging and spectroscopy, measurements were carried out using a scanning electron microscope (Zeiss EVO 50) equipped with a bespoke low magnification CL imaging system (PMT, Hamamatsu R374) and a Gatan MonoCL3 system for UV and visible spectroscopy measurements (PMT: Hamamatsu R943-01; CCD: Princeton Instruments Pixis 100). The sample was sputtered with a thin layer of gold to avoid any charging effects, mounted onto a low temperature stage (Gatan C1002) and held at liquid nitrogen temperature (77 K).

Confocal photoluminescence (PL) imaging was conducted with a home-built room temperature setup using 488 and 532 nm excitation equipped with an oil objective (Zeiss Plan Apo 100x, NA = 1.4). The sample was mounted onto a coplanar waveguide housed on top of a 3-axis piezoelectric stage. Fluorescence was detected on two single photon counters (Excelitas SPCM-NIR) and filtered by an appropriate Semrock transmission filter depending upon the point defect to be imaged. A 50:50 beam splitter partitioned the fluorescence to both detectors, enabling second order photon autocorrelation measurements to be conducted. PL spectra were taken by a fiber coupled spectrometer (ANDOR SR-303i-B). For ODMR measurements, a 20- $\mu\text{m}$  copper wire was placed over the top of the sample for microwave delivery and an external magnetic field applied to the sample via a permanent magnet mounted on a manual five-axis stage.

### III. RESULTS

#### A. Material quality

The material quality is assessed by means of white light cross polarization imaging and white beam x-ray topography (XRT), which show strain and extended defects respectively. We note that this sample contains a small metallic inclusion and a small fracture in the crystal, as shown in Fig. 2. Furthermore, the material shows low internal strain where the average

dislocation density is below  $10^3 \text{ cm}^{-2}$ , and much lower in (001) growth sectors. XRT reveals stacking faults in the {111} growth sectors.

#### B. Impurity and point defect incorporation

EPR measurements indicated that the average concentration of substitutional nitrogen  $[\text{N}_s^0]$  in the sample studied is  $6.5 \pm 1$  ppb. This indicates that in certain growth sectors, at least, the concentration of substitutional nitrogen is higher than the concentration of substitutional boron. The positively charged substitutional nitrogen concentration ( $\text{N}_s^+$ ), as produced by the presence of both the substitutional boron ( $\text{B}_s$ ) acceptor and nitrogen, where  $\text{N}_s^0 + \text{B}_s^0 \rightleftharpoons \text{N}_s^+ + \text{B}_s^-$ , was below infrared detection limits.

Visible CL imaging of the sample, Fig. 3(a), shows cuboctahedral growth, with many minor sectors. Figure 3(b) shows typical low temperature (77 K) cathodoluminescence spectra recorded from the (001) and a {111} growth sector. The emission is dominated by broad bands that have been attributed to donor acceptor pair recombination and unidentified luminescence centers [35–37]; the incorporation efficiency of the impurities and defects varies between different growth sectors giving rise to the contrast in Fig. 3(a). The insets in Fig. 3(b) shows the free exciton (FE) and boron bound exciton (BE) spectra in the (001) and a {111} growth sector, with higher order replica exciton peaks indicated by the \* symbol. The boron BE signal, relative to the FE, observed in low temperature (77 K) CL spectroscopy is used to determine the concentration of substitutional boron impurities [38,39]. The luminescence intensity ratio between the BE and FE is considered proportional to the total shallow acceptor (or donor) concentration, independent of the compensation state of the semiconductor where all shallow impurities are efficiently neutralized under electron injection [40]. In other work a comparison between CL and secondary ion mass spectroscopy indicates that in the



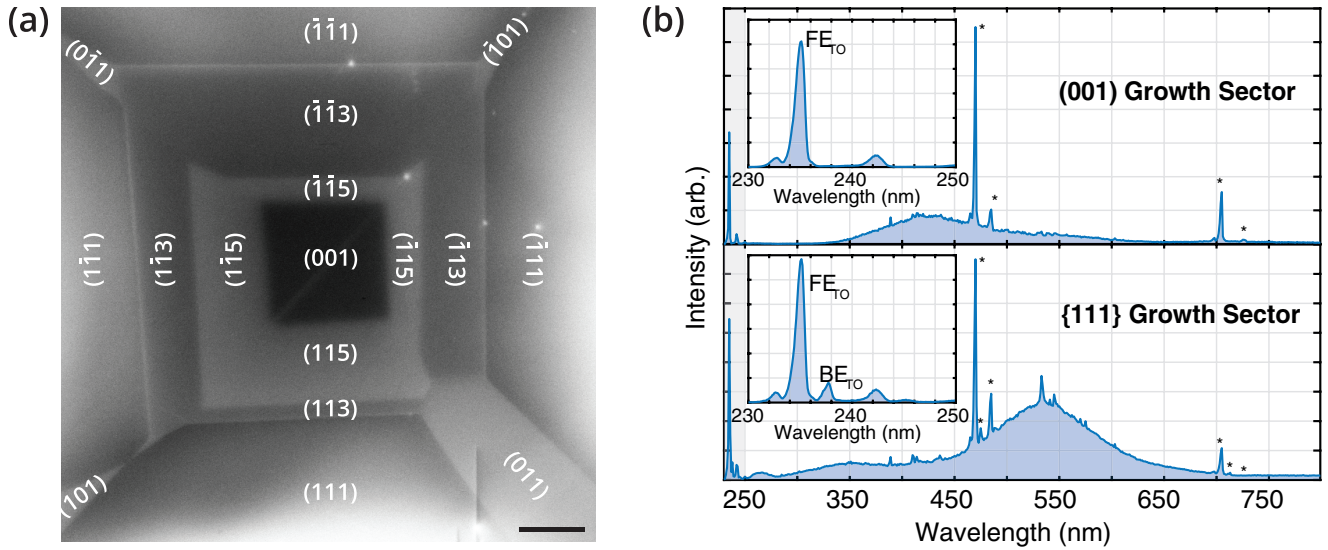


FIG. 3. (a) Low temperature (77 K) cathodoluminescence image (visible light emitted) of the NDT HPHT diamond sample studied. (Scale bar: 200  $\mu\text{m}$ ). (b) Low temperature (77 K) cathodoluminescence spectra recorded in the (001) and a {111} growth sector. The free and bound exciton images are shown in the insets. The higher order replica exciton peaks (higher order monochromator artefacts) are indicated with the \* symbol.

as grown samples all incorporated boron is in the form of substitutional boron [39]. In the system used here, we estimate a detection limit  $<1$  ppb for the substitutional boron acceptor. The boron BE is detected in all growth sectors, except in the (001) sector. The average substitutional boron concentration in each growth sector is given in Table I. The uncertainties quoted in Table I for the boron concentration determined from the ratio of BE to FE include both the measurement error and the variation in boron incorporation within the growth sector.

The survey of the (001) sector does not show any room temperature PL emission associated with defects that are excited by 488 or 532 nm wavelengths. Since the detection limit of the scanning confocal microscope is on the order of  $10^{11} \text{ cm}^{-3}$  ( $10^{-3}$  ppb) for common luminescent point defects in diamond this implies that virtually no (or very few) luminescent point defects are within this sector. By translating the sample and moving from (001) into any {115} and then into any {113} growth sectors, no point defect emission was observed. However, when the sample was translated towards the any {111} growth sector, a locally high concentration of  $\text{NV}^-$  centers was observed at the {111} to {113} growth sector boundary.

Figure 4 shows low temperature visible CL and room temperature confocal PL images of the HPHT diamond sample studied. It was possible to observe several growth sector interfaces within a  $300 \mu\text{m} \times 300 \mu\text{m}$  area, and we find that only

TABLE I. Average substitutional boron concentration (ppb) in the growth sectors as determined by low temperature (77 K) CL spectroscopy.

[B] (ppb)	Growth sector				
	(001)	{011}	{115}	{113}	{111}
	$< 1$	$19 \pm 3$	$2 \pm 1$	$9 \pm 2$	$84 \pm 10$

the {111} to {113} growth sector boundaries exhibit fluorescence associated with  $\text{NV}^-$ . The room temperature confocal PL images shown in Fig. 4 were recorded with a 640-nm-long pass filter (to pass the emission from the  $\text{NV}^-$  defects) and the identity of the  $\text{NV}^-$  defects decorating the {111} to {113} growth sector boundaries was confirmed by ODMR and PL spectroscopy. Interestingly the boundaries between certain {111} and {113} sectors are associated with the appearance of “parallel lines” of strong  $\text{NV}^-$  defect emission in the  $\text{NV}^-$  PL maps (Fig. 4, location B and C).

To investigate the evolution of these decorated growth sector boundaries during growth, individual XY PL images (with 640-nm-long pass filter; XY is in the plane of the sample plate, Z is depth through the plate) were recorded at a 15 different depths in the sample plate (defined by the overlapping laser excitation and detection volumes) and this image plane stepped from the surface to a depth of approximately  $15 \mu\text{m}$  at a  $1\text{-}\mu\text{m}$  pitch. These images were stacked to produce a three-dimensional (3D) image, and subsequent XZ PL images were constructed by slicing the 3D volume through the appropriate planes. The diffraction limited resolution of the microscope in the Z direction was measured to be  $1.15 \mu\text{m}$ , in good agreement with theory (similarly measured resolution in XY plane was measured to  $0.33 \mu\text{m}$ ).

The XZ maps shown in Fig. 5 indicate that the  $\text{NV}^-$  decoration was restricted to narrow regions that follow the sector boundaries, without incorporation of  $\text{NV}^-$  in to the bulk growth sectors.

Spectra collected around these interfaces identify three different point defects:  $\text{NV}^-$ ;  $\text{SiV}^-$  (PL emission at 737 nm); and PL emission centered on 884 nm. The latter is attributed to a nickel-related defect [41,42] labeled previously as both the 1.40-eV defect [43] and NIRIM-2 [44], and is known to be a paramagnetic ( $S = 1/2$ ) defect of trigonal ( $C_{3v}$ ) symmetry [41,45]. While there are many nickel related defects identified in diamond, a survey of the literature on the 1.40-eV defect

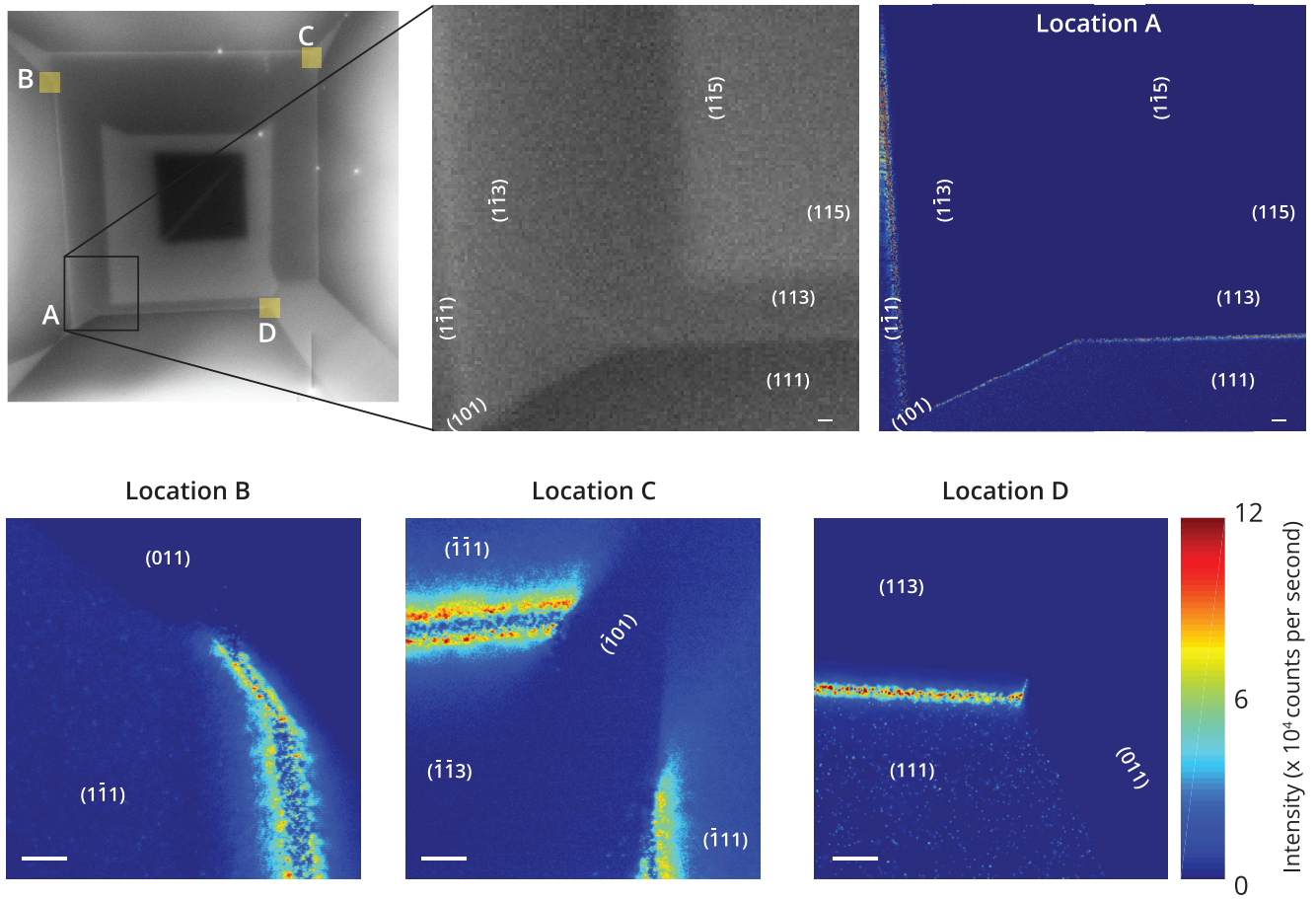


FIG. 4. (a) CL image reported in Fig. 3(a) but now labeled with four regions (A, B, C, and D) where room temperature confocal PL images have been recorded. (b) A small region of the CL image, as indicated, with the different growth sectors labeled. (c) Room temperature confocal PL image recorded with a 640-nm long pass filter (to pass the emission from the NV<sup>-</sup> defects) in the same region as (b). The {111}/{113} growth sector boundaries are decorated with NV<sup>-</sup> defects (identity of the NV<sup>-</sup> defects confirmed by ODMR and localized luminescence spectroscopy measurements, see text for details). (d), (e), and (f) show room temperature confocal PL images recorded with a 640-nm long pass filter for the locations labeled B, C, and D in (a). It is clear from (d), (e), and (f) that only the {111}/{113} growth sector boundaries are decorated with NV<sup>-</sup> defects. (Scale bar; 10 μm).

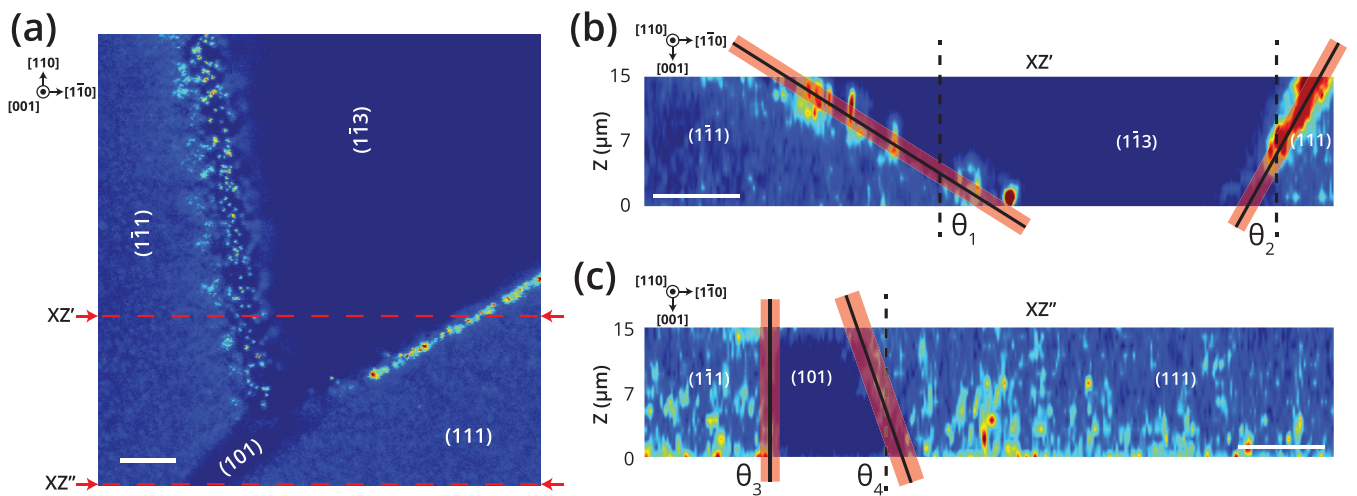


FIG. 5. (a) 80 μm × 80 μm confocal image at a depth of 7 μm from the surface of the sample at location A (Fig. 4). Two locations are marked for the XZ slices. (b) and (c) are the resultant planar slices for XZ' and XZ'' respectively. The angles labeled are between the vertical ([001] direction) and the line shown:  $\theta_1 = 55^\circ \pm 5^\circ$ ,  $\theta_2 = 30^\circ \pm 5^\circ$ ,  $\theta_3 = 0^\circ \pm 5^\circ$ , and  $\theta_4 = 19^\circ \pm 10^\circ$ . (Scale bar; 10 μm).

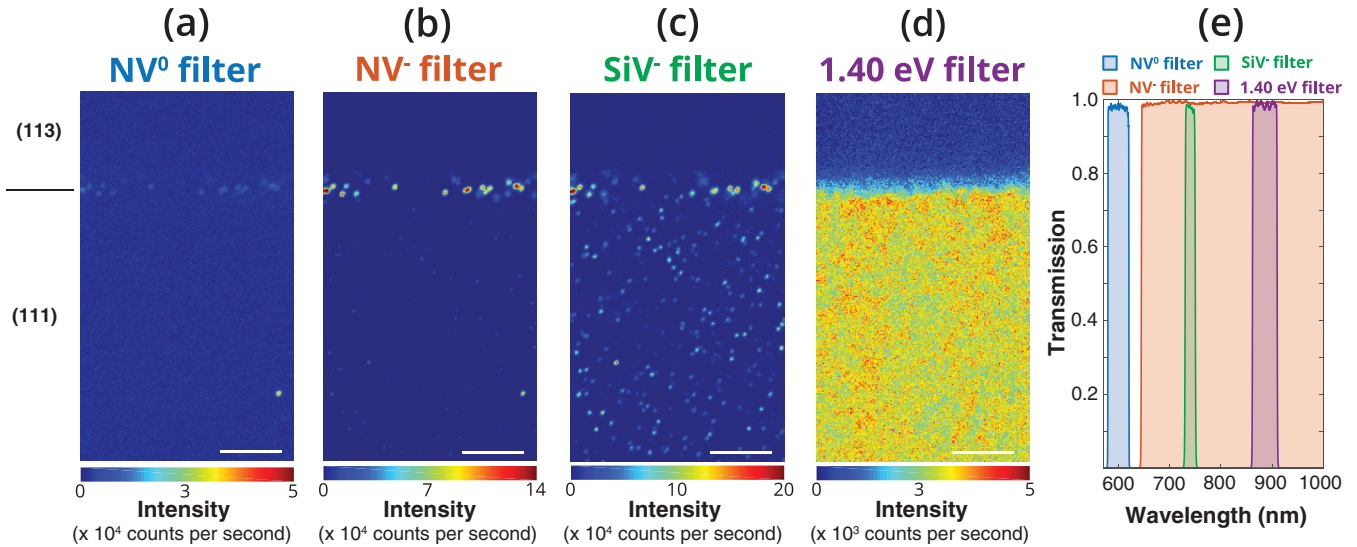


FIG. 6. Employing optical filters matched to the emission range of each defect, the spatial distribution of each defect at the {113} to {111} sector interfaced can be mapped. (a) NV<sup>0</sup>, (b) NV<sup>-</sup> (c) SiV<sup>-</sup> (with  $\sim 10\%$  NV<sup>-</sup>), and (d) 1.40-eV defect. The transmission profile of each filter is given in (e). For the 1.40-eV defect shown in (d), the 532-nm excitation power was increased to 100 mW, c.f. 5 mW for the other defect distribution maps in this figure. (Scale bar; 5  $\mu\text{m}$ ).

highlights that its atomic structure has not yet been definitively identified and so we will continue to refer to it as the 1.40-eV defect from this point forward.

The spatial distribution of each defect close to the {113} and {111} interface can be identified by luminescence mapping using optical filters matched to the emission range of each defect (Fig. 6). These maps reveal that the incorporation of defects is inhomogeneous, such that the boundary between {111} and {113} growth sectors is decorated only with NV<sup>-</sup> centers, whereas only the bulk {111} sectors contain both SiV<sup>-</sup> and 1.40-eV defects [43,46]. It should be noted that the filters are not 100% selective for each defect; for example, the SiV<sup>-</sup> filter will also pass approximately 10% of the emission from the vibronic side band of NV<sup>-</sup> defects.

### C. Orientation of incorporated defects

The number of defects detected by PL within a diffraction-limited optical volume can be quantified by performing second-order photon autocorrelation measurements ( $g^2$ ) [24], so long as that number is small ( $<2-4$ ). Given the diffraction limited PL excitation/detection volume of a confocal microscope, detection of single defects in diamond requires a bulk defect concentration on the order of  $1.76 \times 10^{12} \text{ cm}^{-3}$  ( $10^{-2}$  ppb) or lower to ensure individual defects can be optically isolated.  $g^2$  measurements at several {111} to {113} growth sector boundaries indicated that where the region of NV<sup>-</sup> decoration is wider than  $\sim 3 \mu\text{m}$ , individual NV<sup>-</sup> centers could be optically detected (excitation/detection volume a few  $\mu\text{m}$  beneath the surface); otherwise ensembles of NV<sup>-</sup> defects were observed indicating that local concentration of NV<sup>-</sup> centers is higher than approximately  $10^{-2}$  ppb.

For a {111}–{113} growth sector boundary with an NV<sup>-</sup> decoration width of  $\sim 5 \mu\text{m}$  (Fig. 7), 78% of the NV centers detected were single defects (e.g., only one NV<sup>-</sup> defect per excitation/detection volume). It is possible to identify the

orientation of a given NV<sup>-</sup> center by applying an arbitrarily oriented magnetic field and measuring the ODMR spectrum: this will identify if there is any preferential (e.g., not random with respect to the possible symmetry related orientations) defect alignment [22,23]. Measurements on 100 individual NV<sup>-</sup> centers [in the region identified by the dashed white line in Fig. 7(a)], revealed that all four possible orientations of the NV<sup>-</sup> centers occurred with equal probability (0.25) in this region indicating no preferential orientation/alignment.

Room temperature ODMR on SiV<sup>-</sup> and the 1.40-eV defect have not been previously reported, therefore we investigated possible preferential alignment of both defects by a rotation of the linear excitation polarization. The 737-nm zero phonon line (ZPL) of SiV<sup>-</sup> is an E  $\leftrightarrow$  E optical transition [47] (ignoring the small spin-orbit splitting) and the 1.40-eV defect 884 nm ZPL is an A  $\leftrightarrow$  E optical transition [45]. Both defects are trigonal symmetry defects, and hence the rotation of the linear excitation polarization will produce a fluorescence intensity modulation that is well understood [47–51].

Optical polarization measurements were conducted by rotating the electric field vector of the excitation laser from  $E||[1\bar{1}0]$  (horizontal polarization) to  $E||[110]$  (vertical polarization). SiV<sup>-</sup> showed equal contrast in two {111} sectors indicating a nonpreferential alignment with respect to the growth direction (Fig. 8). However, the 1.40-eV defect responds differently such that one sector favored maximal emission by vertical polarization and the other sector by horizontal polarization. We note that the concentration of the 1.40-eV defects in the two {111} sectors is different, as judged by the maximum emission intensity.

## IV. DISCUSSION

### A. Growth sectors and the nitrogen and boron incorporation

HPHT diamond crystals grown from solutions consist of (growth) sectors grown in discrete directions defined by the



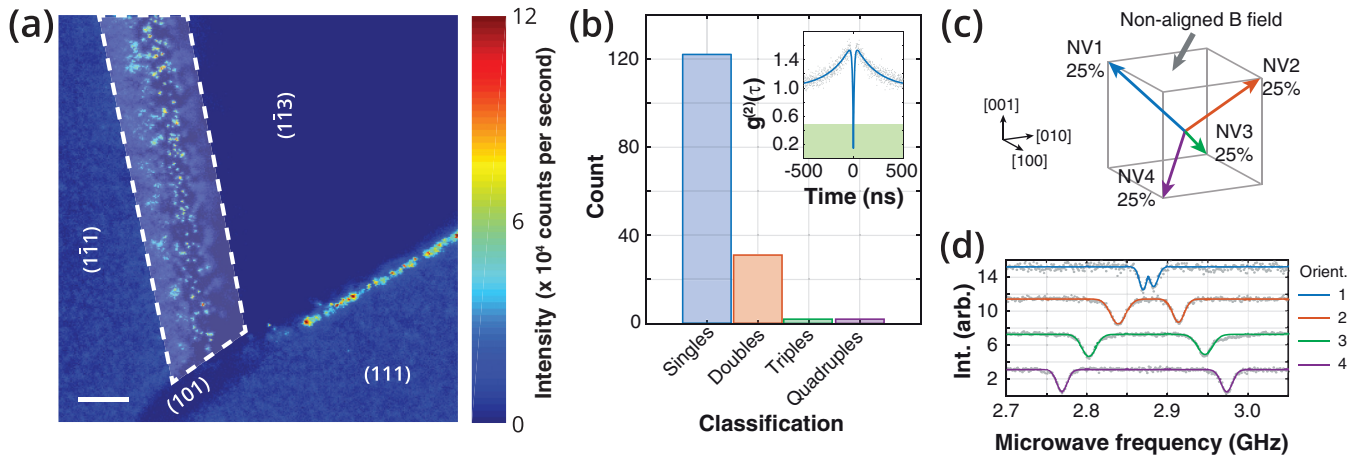


FIG. 7. (a) Optically detected magnetic resonance (ODMR) study at location A (Fig. 4) (Scale bar; 10  $\mu\text{m}$ ). (b) Classification histogram of  $\text{NV}^-$  centers based on their photon autocorrelation minima with a representative measurement for a single center (inset). (c) The four possible trigonal orientations along  $\langle 111 \rangle$  for the  $\text{NV}^-$  center with the measurement occurrence from ODMR in this study. (d) Single center ODMR spectra showing the measured fluorescence intensity (data points) as a function of microwave frequency for the differently oriented  $\text{NV}^-$  defects in a magnetic field applied such that the vector specifying its orientation makes a different angle with each of the four symmetry axes of the individual defects. The solid curves show fits to the spin Hamiltonian for the differently orientated defects.

normal of the crystal faces involved. The final crystal exhibits only those faces that have low growth velocities since those with higher growth rates grow out and the external morphology is dominated by the slower growing sectors. It is well known that in HPHT diamond the incorporation probability

for nitrogen and boron varies between growth sectors and that the actual uptake of impurities is influenced by the details of the growth conditions at each growth interface of the growing crystal [7]. Growth sectors are separated by growth-sector boundaries, which are internal surfaces over which the edges

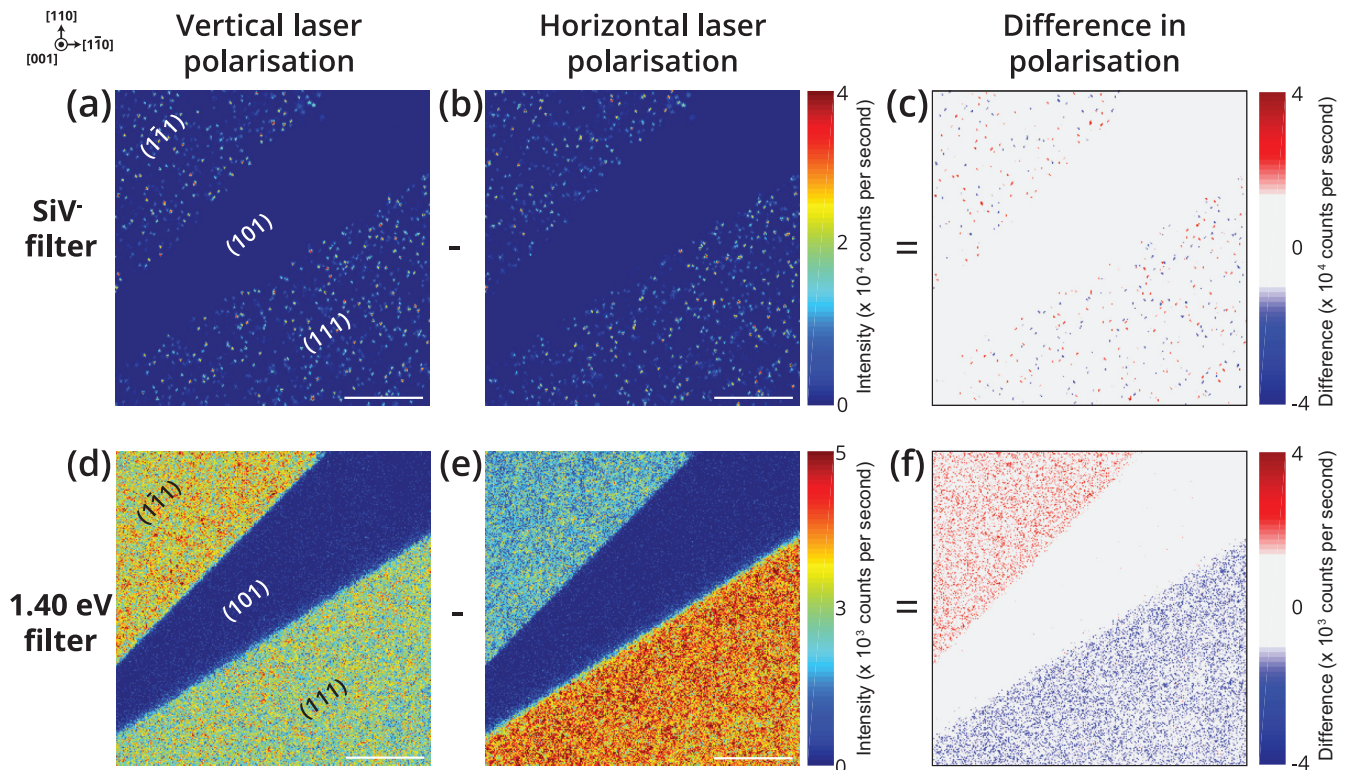


FIG. 8. The effect of laser polarization (vertical or horizontal) on both  $\text{SiV}^-$ , (a) and (b), respectively, and the 1.40-eV defect, (d) and (e), respectively. By taking the difference in intensity due to laser polarization it is clear to see in (c) that  $\text{SiV}^-$  does not exhibit any preferential orientation, whereas there is a clear correlation in (f) for the 1.40-eV defect to indicate this defect has grown in with a preferred orientation (parallel to the sector growth direction). (Scale bar; 10  $\mu\text{m}$ ).

between neighboring sectors have passed during growth [52]. The local direction of a growth-sector boundary depends on the relative growth velocity of the neighboring faces. If the relative velocity is constant the boundary is planar, but if not the boundary can be an irregular internal surface. In HPHT diamond the fast growing {110} sectors often have irregular surfaces with neighboring slower growing {100} and {111} sectors [3]. The growth-sector boundaries and the surrounding regions may be indistinguishable from the bulk sectors in terms of defect and impurity incorporation, however, there may be increased local impurity and defect incorporation when growth layers on neighboring faces meet.

It is shown that the incorporation of boron into the studied (001) sector of the HPHT diamond is less than 1 ppb (Table I). The large variation of boron concentration between growth sectors is consistent with published data [7,53,54] where it was shown that the boron is incorporated in the greatest concentrations in the {111} sectors, then in the {110} sectors, and in lower concentrations in {113}, {115}, and {001} sectors. Our results and those of Klepikov *et al.* [53] suggest that the boron concentration is lowest in the {001} sector, and very much less ( $<1/100$ ) than in the {111} sector.

In this sample, the  $N_s^0$  concentration is well below the detection limit of SIMS. Since the concentration of  $N_s^0$  determined by EPR is an average over the whole sample it is difficult to know for certain the  $N_s^0$  concentration in an individual growth sector. However, from the boron concentrations present in this sample (Table I) we make the assumption that the nitrogen is mostly compensated (e.g., predominately in the form of  $N_s^+$ , which is not detected by EPR) in the {111} growth sectors, which contributes 69% of the sample volume, but then only a fraction is compensated in the remaining sectors. By approximating the volume occupied by each growth sector, and allowing the relative growth sector incorporation ratio of the  $N_s^0$  concentration to follow that determined by Burns *et al.* [7], the measured EPR signal for  $N_s^0$  is reached if the uncompensated concentration in the (001) growth sector is  $\sim 50$  ppb. No  $NV^-$  defects were detected in a  $200 \times 200 \mu\text{m}$  region of the (001) growth sector by confocal PL microscopy of the as grown material, thus if the  $N_s^0$  concentration is  $\sim 50$  ppb then we can infer that in the (001) growth sector the incorporation of  $N_s^0$  is  $\gg 10^6$  times more likely than a  $NV^-$  defect. Subsequent electron irradiation (4.5 MeV electrons) and annealing at 800 °C after this initial study resulted in very strong NV PL emission from the (001) growth sector, shown in the Supplemental Material [71], as expected for vacancy capture at  $N_s^0$  defects.

The properties of the cube sector are potentially exciting for  $NV^-$ -based quantum technologies: given the low background boron contamination of {001} growth sectors, we are optimistic that  $NV^-$  defects introduced into this material by ion implantation or femtosecond laser writing [55] would have very attractive properties that would not be compromised by grown-in strain given the very low concentration of dislocations. Even if the  $N_s^0$  concentration were as high as  $\sim 100$  ppb, we would expect the spin decoherence of any  $NV^-$  defects introduced to be limited by interaction with the natural abundance  $^{13}\text{C}$ , rather than the residual nitrogen. If the  $N_s^0$  contamination of {001} growth sectors could be reduced to less than 1 ppb then this HPHT material may

even outperform “quantum grade” CVD diamond in certain applications.

### B. Significance of NV decoration at the {111} to {113} growth sector boundary.

The orientation of a growth sector boundary is dependent on the relative growth velocity of the two neighboring crystal faces involved. The boundary is straight when the relative growth rate is constant, and curved when it changes due to fluctuations in the growth conditions. The relative growth rate can be determined if the growth-sector boundary is visible and the growth direction of the adjacent crystal faces can be identified [52]. The region shown in Fig. 5(a) is particularly complicated as there is growth in several different directions. Taking a linear growth rate in {111} and {113} directions for HPHT synthesis at 1500 °C of  $\sim 50 \mu\text{m}/\text{h}$  [56] would suggest that since the decoration of the growth sector boundary appears straight in Fig. 5, the different sector growth rates were stable over tens of minutes.

The cross product of the vectors normal to the intersecting planes gives a vector in the plane of the growth sector boundary, and the direction of travel of the boundary is determined from the growth velocities of the two planes. From these two vectors (direction of travel of the boundary and cross product of two intersecting planes) the plane of the growth sector boundary can be determined. In Fig. 4, location A, where the observation direction is along  $\sim [001]$ , the boundary between (113)–(111) and  $(1\bar{1}3)$ –(111) growth sectors will be independent of the relative growth velocities and orientated along  $[1\bar{1}0]$  (horizontal) and  $[110]$  (vertical) directions, respectively.

The decorated boundary between  $(1\bar{1}3)$ –(111) indicates  $v_{1\bar{1}3}/v_{111} \approx 1.13$ , where  $v_{l_{mn}}$  is the linear growth velocity. In Fig. 5(b), the angle between the decorated boundary and the vertical  $[001]$  suggests that  $v_{1\bar{1}3}/v_{1\bar{1}1} \approx 0.87$  and  $v_{1\bar{1}3}/v_{111} \approx 1.14$  with the latter value in good agreement with the result for the  $[001]$  direction of observation. From Fig. 5(c), even though the boundaries are not decorated, the sector dependent defect incorporation allows us to estimate that  $v_{101}/v_{1\bar{1}1} \approx 1.2$  and  $v_{101}/v_{111} \approx 0.94$ , but in the latter case the uncertainty is very large. Since there is no knowledge of where the plate was cut from the grown crystal, or its final morphology, it would be unwise to further analyze growth rate data noting this study represents only a small time window during growth.

The orientation of the decorated {111}–{113} growth sector boundaries with respect to the  $[001]$  viewing direction impacts on whether single NV centers can be observed at the growth sector boundary. In the configuration used here spatial resolution of the confocal PL microscope in Z is approximately  $3.4 \times$  worse than in X or Y. Even if we assume that the local density of NV centers at all {111} to {113} growth sector boundaries is the same and the decoration extends from the boundary a distance much less than the confocal resolution in depth, then the confocal excitation/detection volume is less like to contain multiple NV defects if the growth sector boundary the makes a large angle with the viewing direction. This is clear in Fig. 5 where the  $(1\bar{1}3)$  sector intersects with the  $(1\bar{1}1)$  and (111) sectors. Furthermore, the local direction of the growth sector boundary depends on the instantaneous relative growth velocity of the neighboring faces, so for a



TABLE II. The minimum angle, in degrees, that can occur between two neighboring growth sectors.

	Growth Sector Boundary			
	{111}–{113}	{111}–{011}	{113}–{115}	{115}–{001}
Minimum angle	29.5°	35.3°	9.4°	15.8°

boundary where the relative growth rates vary it is possible that the decoration could be more complicated. Such a variation may explain the subtle differences in decoration observed for different {111} to {113} growth sector boundaries in Fig. 4. Note the CL image (Fig. 3) indicates that all {113} growth sectors have different growth rates and therefore plausible that the density of NV centers at the growth sector boundary may vary with the absolute and relative growth rates.

It is interesting to consider the significance of the fact that only the {113}–{111} growth sector interface is decorated with NV<sup>-</sup> defects. This transition zone between the {113} and {111} planes is seen in the visible CL image [Fig. 3(a)] as a band of higher intensity emission, where the confocal maps correlate the width of these growth sector interfaces to the width of NV<sup>-</sup> decoration. The minimum angle change that can occur between two neighboring growth sectors is outlined in Table II. It is possible that is not energetically favorable for the crystal to grow with a direct transition of {113}–{111} (or {111}–{110}) and must do so via small steps with higher order crystallographic planes with subsequent increased incorporation of nitrogen and NV<sup>-</sup> defects at the {113}–{111} boundary. However, kinetic and impurity absorption effects may well influence the nature of the transition and it will require further work to determine why only the {113}–{111} growth sector boundary is decorated with NV<sup>-</sup> defects.

Finally, the decoration of {111}–{113} growth sector boundaries is not unique to the material produced by NDT. We observe a similar growth sector boundary decoration in material grown by another HPHT supplier using a different solvent-catalyst and getter chemistry (see the Supplemental Material [71]). Therefore, the reported decoration is relatively insensitive to the process conditions in gettered type IIa HPHT material.

### C. The lack of NV preferential orientation

Preferential orientation of grown-in defects has been observed in both CVD- [34,57] and HPHT- [51,58] grown diamond, with some theoretical work carried out to investigate the surface kinetics and chemistry required to produce defect preferential orientation [59]. In the specific case of the NV<sup>-/0</sup> defect, there are numerous reports of preferential alignment during CVD growth on ⟨110⟩, ⟨113⟩, and ⟨111⟩ oriented substrates [22,23,34]. Destruction of preferential orientation has also been demonstrated by annealing samples at temperatures high enough to allow the defect in question to reorientate [60].

There are two plausible explanations for the lack of preferential orientation of the NV centers:

(i) The NV defect did not grow in as a unit but was formed by vacancies migrating to substitutional nitrogen defects to produce defects in all possible orientations.

(ii) Preferential orientation did occur during growth, but the growth temperature was high enough to enable reorientation of NV centers during the growth run without all the defects annealing out.

The sample studied has spent time at elevated temperatures in the growth capsule. Typical catalyst-solvent HPHT diamond growth temperatures are 1350–1600 °C [54]. The degree to which a defect “X” may undergo reorientation can be modeled by first-order chemical kinetics. Using an activation energy  $E_A \approx 4.0$  eV and attempt frequency  $\nu \approx 10^{11}$  s<sup>-1</sup> for NV [61], we find that no appreciable preferential orientation remains after only a few minutes (seconds) at 1350 °C (1500 °C). It is, therefore, reasonable to expect that any initial preferential orientation of NV would have annealed back to equilibrium populations during the time the sample spent at elevated temperatures even if the material studied was grown towards the end of the growth run. Using the values published by Pinto *et al.* [62] for the activation energy of NV migration and attempt frequency, any NV preferential orientation would be lost in under 1 min at 1500 °C. Thus the lack of observed preferential orientation of NV centers is consistent with our understanding of the thermal reorientation of this defect. The one report of preferentially aligned NV centers produced in {111} growth sectors during HPHT growth [47] (orientation parallel to growth direction is missing) is at odds with our understanding.

The NV defect reorients locally before it dissociates/migrates and interacts with other defects and impurities. It is well known that as NV anneals out the dinitrogen vacancy defect N<sub>2</sub>V is produced presumably by the reaction  $NV + N_s \rightarrow N_2V$  [61,63,64]. N<sub>2</sub>V<sup>0</sup> gives rise to the H3 absorption/emission (ZPL 503 nm) and N<sub>2</sub>V<sup>-</sup> to the H2 absorption/emission (ZPL 982 nm) and a characteristic EPR spectrum [65]. No H3 emission was detected using 488-nm excitation in any region of the sample using confocal PL. This suggests an upper limit for the growth temperature of 1500 °C since at this temperature, H3 could be produced [61].

### D. Preferential orientation of SiV<sup>-</sup> and the 1.40-eV defect

The preferential orientation of the 1.40-eV defect observed in the {111} growth sectors has been previously reported [60,66]. The sector-dependent contrast follows an approximate 3:1 intensity contrast ratio for the 1.4-eV emission that would be expected for 100% preferential alignment of the symmetry axis of a trigonal defect (A ↔ E optical transition) along the growth direction of each of the respective {111} sectors and hence is clear evidence that this defect is indeed preferentially orientated. This HPHT diamond was synthesized in a Co-Fe-C system. Previous reports using the Co-Fe-C system with additives of titanium [67] or zirconium [68] to reduce nitrogen incorporation in the grown diamond

have shown that high-quality diamond crystals can be produced. Thus, the observation of the 1.40-eV defect in the {111} growth sectors of the diamond leads us to suppose that the growth system was contaminated with nickel. We note that if the concentration of the 1.40-eV defect were as low as  $\sim 0.1$  ppb there would still be  $\sim 20$  defects in the confocal PL volume. Thus, if the nickel is readily incorporated the contamination of the growth system could be at trace amounts.

The absence of any preferential orientation of the  $\text{SiV}^-$  centers is unexpected. Preferential alignment has been previously predicted by first-principles calculations [69] and observed experimentally in CVD diamond doped with silicon [47,57]. In CVD grown diamond it has been suggested that like  $\text{NV}^-$ , the  $\text{SiV}^-$  defect is grown in as a unit [57]. With regards to the reorientation of the  $\text{SiV}^-$  centers during growth, little is known about the migration energies involved, but even at temperatures as high as 1900 °C the  $\text{SiV}^-$  fluorescence intensity does not reduce significantly [70], with preferential orientation of  $\text{SiV}^0$  persisting in CVD diamond annealed up to 2000 °C [57], indicating that the defect is stable well above the anticipated HPHT growth temperature. The  $\text{SiV}^-$  defects observed in the {111} growth sectors of the HPHT diamond do not appear to be preferentially orientated, although we note a previous report suggesting that the orientation parallel to the [111] growth direction was missing in the HPHT diamond studied [47]. Further studies on the incorporation mechanism of  $\text{SiV}^-$  during HPHT synthesis is required with regards to the lack of preferential orientation in {111} sectors.

## V. CONCLUSIONS

HPHT-synthesized diamond from NDT has been studied with confocal PL microscopy. In this material we find three species of point defects;  $\text{NV}^-$ ,  $\text{SiV}^-$ , and nickel-related emission centered on 884 nm, which we refer to in this paper as the 1.40-eV defect. Confocal imaging reveals sector interfaces between {113} and {111} are decorated with  $\text{NV}^-$  centers. We note that this decoration has now also been seen in type II HPHT diamonds produced by other laboratories; in all the high purity HPHT material studied to date decoration

of {113} and {111} boundaries with  $\text{NV}^-$  centers is always observed. This decoration allows for determination of the relative growth rates of the neighboring {113} and {111} growth sectors. The bulk {111} sectors in the sample studied here exhibit emission from only  $\text{SiV}^-$  and 1.40-eV defects when excited with 532-nm light. There is no evidence to suggest preferential orientation for either the  $\text{NV}^-$  or  $\text{SiV}^-$  defects although it is evident that the 1.40-eV defect is grown-in with the trigonal axis of the defect aligned with the [111] growth direction, in line with previously published results. At the HPHT growth temperature, the  $\text{NV}^-$  defect is expected to rapidly reorientate so no preferential orientation is expected even if the defect grew in as a unit on, for example, a {111} growth surface but a further understanding is required for the incorporation of  $\text{SiV}^-$ .

The high crystalline quality of this material coupled with its high purity, resulting in a low point defect density, reflects the recent strides made in HPHT diamond synthesis methods. Future work will focus on investigating the native NV centers for their suitability for quantum applications and how this material compares to HPHT diamond grown in different process conditions.

## ACKNOWLEDGMENTS

This work was supported by the EPSRC Centre for Doctoral Training in Diamond Science and Technology (Grant No. EP/L015315/1) and funding from the Gemological Institute of America for a Ph.D. studentship for PLD. B.L.G. and M.E.N. acknowledge funding from NICOP (Grant No. N62909-16-1-2111-P00002 - Towards a Picotesla DC Diamond Magnetometer) and NQIT (Grant No. EP/M013243/1 - UK Quantum Technology Hub: NQIT - Networked Quantum Information Technologies). B.L.G. acknowledges funding from the Royal Academy of Engineering. The authors thank A.V. Koliadin, N.T. Khikhashvili, R.V. Isakov, and Y.A. Loguinov at New Diamond Technology for the growth of this sample, and D. J. F. Evans at De Beers Group Technology, UK for providing assistance with cathodoluminescence imaging and spectroscopy.

- 
- [1] J. Achard, F. Silva, O. Brinza, A. Tallaire, and A. Gicquel, *Diam. Relat. Mater.* **16**, 685 (2007).
  - [2] Y. N. Palyanov, Y. M. Borzdov, A. F. Khokhryakov, I. N. Kupriyanov, and A. G. Sokol, *Cryst. Growth Des.* **10**, 3169 (2010).
  - [3] R. C. Burns, A. I. Chumakov, S. H. Connell, D. Dube, H. P. Godfried, J. O. Hansen, J. Härtwig, J. Hozzowska, F. Masiello, L. Mkhonza, M. Rebak, A. Rommevaux, R. Setshedi, and P. Van Vaerenbergh, *J. Phys. Condens. Matter* **21**, 364224 (2009).
  - [4] U. F. S. D'Haenens-Johansson, A. Katrusha, K. S. Moe, P. Johnson, and W. Wang, *Gems Gemol.* **51**, 260 (2015).
  - [5] Y. N. Palyanov, I. N. Kupriyanov, A. F. Khokhryakov, and V. G. Ralchenko, in *Handbook of Crystal Growth*, edited by P. Rudolph (Elsevier, Amsterdam, 2015), Vol. 2a, pp. 671–713.
  - [6] M.-L. T. Rooney, *J. Cryst. Growth* **116**, 15 (1992).
  - [7] R. C. C. Burns, V. Cvetkovic, C. N. N. Dodge, D. J. F. J. F. Evans, M.-L. T. Rooney, P. M. M. Spear, and C. M. M. Welbourn, *J. Cryst. Growth* **104**, 257 (1990).
  - [8] P. W. May, *Philos. Trans. R. Soc. London Ser. A* **358**, 473 (2000).
  - [9] E. Anoinik, A. Muhr, A. Bennett, D. Twitchen, and H. de Wit, in *Components Packaging Laser System*, edited by A. L. Glebov and P. O. Leisher, in Proc. SPIE 9346 (SPIE, New York, 2015), p. 93460T.
  - [10] G. Gantenbein, A. Samartsev, G. Aiello, G. Dammertz, J. Jelonnek, M. Losert, A. Schlaich, T. A. Scherer, D. Strauss, M. Thumm, and D. Wagner, *IEEE Trans. Electron Devices* **61**, 1806 (2014).
  - [11] Y. Meng, C. Yan, S. Krasnicki, Q. Liang, J. Lai, H. Shu, T. Yu, A. Steele, H. Mao, and R. J. Hemley, *Phys. Status Solidi A* **209**, 101 (2012).

- [12] F. Jelezko and J. Wrachtrup, *New J. Phys.* **14**, 105024 (2012).
- [13] M. L. Markham, J. M. Dodson, G. A. Scarsbrook, D. J. Twitchen, G. Balasubramanian, F. Jelezko, and J. Wrachtrup, *Diam. Relat. Mater.* **20**, 134 (2011).
- [14] R. S. Balmer, J. R. Brandon, S. L. Clewes, H. K. Dhillon, J. M. Dodson, I. Friel, P. N. Inglis, T. D. Madgwick, M. L. Markham, T. P. Mollart, N. Perkins, G. A. Scarsbrook, D. J. Twitchen, A. J. Whitehead, J. J. Wilman, and S. M. Woollard, *J. Phys. Condens. Matter* **21**, 364221 (2009).
- [15] A. Tallaire, J. Achard, F. Silva, O. Brinza, and A. Gicquel, *CR Phys.* **14**, 169 (2013).
- [16] M. Schreck, M. Mayr, O. Klein, M. Fischer, S. Gsell, A. F. Sartori, and B.-C. Gallheber, *Phys. Status Solidi* **213**, 2028 (2016).
- [17] H. Sumiya, K. Harano, and K. Tamasaku, *Diam. Relat. Mater.* **58**, 221 (2015).
- [18] S. Stoupin, S. Antipov, J. E. Butler, A. V. Kolyadin, and A. Katrusha, *J. Synchrotron Radiat.* **23**, 1118 (2016).
- [19] A. Tallaire, V. Mille, O. Brinza, T. N. Tran Thi, J. M. Brom, Y. Loguinov, A. Katrusha, A. Koliadin, and J. Achard, *Diam. Relat. Mater.* **77**, 146 (2017).
- [20] B. Deljanin, C. S. Canadian, M. Alessandri, and A. Peretti, *Contrib. Gemol.* **15**, 1 (2015).
- [21] I. Aharonovich, S. Castelletto, D. A. Simpson, C.-H. Su, A. D. Greentree, and S. Praver, *Rep. Prog. Phys.* **74**, 076501 (2011).
- [22] J. Michl, T. Teraji, S. Zaiser, I. Jakobi, G. Waldherr, F. Dolde, P. Neumann, M. W. Doherty, N. B. Manson, J. Isoya, and J. Wrachtrup, *Appl. Phys. Lett.* **104**, 102407 (2014).
- [23] M. Lesik, T. Plays, A. Tallaire, J. Achard, O. Brinza, L. William, M. Chipaux, L. Toraille, T. Debuisschert, A. Gicquel, J. F. Roch, and V. Jacques, *Diam. Relat. Mater.* **56**, 47 (2015).
- [24] F. Jelezko and J. Wrachtrup, *Phys. Status Solidi* **203**, 3207 (2006).
- [25] Y.-C. Chen, P. S. Salter, S. Knauer, L. Weng, A. C. Frangeskou, J. Colin, P. R. Dolan, S. Johnson, B. L. Green, G. W. Morley, M. E. Newton, J. G. Rarity, M. J. Booth, and J. M. Smith, *Nat. Photon.* **11**, 77 (2017).
- [26] Y. Chu, N. P. de Leon, B. J. Shields, B. Hausmann, R. Evans, E. Togan, M. J. Burek, M. Markham, A. Stacey, A. S. Zibrov, A. Yacoby, D. J. Twitchen, M. Loncar, H. Park, P. Maletinsky, and M. D. Lukin, *Nano Lett.* **14**, 1982 (2014).
- [27] R. Alléaume, F. Treussart, G. Messin, Y. Dumeige, J.-F. Roch, A. Beveratos, R. Brouri-Tualle, J.-P. Poizat, and P. Grangier, *New J. Phys.* **6**, 92 (2004).
- [28] L. Rondin, J.-P. Tetienne, T. Hingant, J.-F. Roch, P. Maletinsky, and V. Jacques, *Rep. Prog. Phys.* **77**, 056503 (2014).
- [29] S. Kolkowitz, A. Safira, A. A. High, R. C. Devlin, S. Choi, Q. P. Unterreithmeier, D. Patterson, A. S. Zibrov, V. E. Manucharyan, H. Park, and M. D. Lukin, *Science* **347**, 1129 (2015).
- [30] D. M. Toyli, C. F. de las Casas, D. J. Christle, V. V. Dobrovitski, and D. D. Awschalom, *Proc. Natl. Acad. Sci.* **110**, 8417 (2013).
- [31] M. W. Doherty, V. V. Struzhkin, D. A. Simpson, L. P. McGuinness, Y. Meng, A. Stacey, T. J. Karle, R. J. Hemley, N. B. Manson, L. C. L. Hollenberg, and S. Praver, *Phys. Rev. Lett.* **112**, 047601 (2014).
- [32] B. Hensen, H. Bernien, A. E. Dreau, A. Reiserer, N. Kalb, M. S. Blok, J. Ruitenber, R. F. L. Vermeulen, R. N. Schouten, C. Abellan, W. Amaya, V. Pruneri, M. W. Mitchell, M. Markham, D. J. Twitchen, D. Elkouss, S. Wehner, T. H. Taminiau, and R. Hanson, *Nature (London)* **526**, 682 (2015).
- [33] P. C. Humphreys, N. Kalb, J. P. J. Morits, R. N. Schouten, R. F. L. Vermeulen, D. J. Twitchen, M. Markham, and R. Hanson, *Nature (London)* **558**, 268 (2018).
- [34] A. M. Edmonds, U. F. S. D'Haenens-Johansson, R. J. Cruddace, M. E. Newton, K. M. C. Fu, C. Santori, R. G. Beausoleil, D. J. Twitchen, and M. L. Markham, *Phys. Rev. B* **86**, 035201 (2012).
- [35] J. A. Freitas, P. B. Klein, and A. T. Collins, *Appl. Phys. Lett.* **64**, 2136 (1994).
- [36] P. B. Klein, M. D. Crossfield, J. A. Freitas, and A. T. Collins, *Phys. Rev. B* **51**, 9634 (1995).
- [37] S. C. Lawson, H. Kanda, H. Kiyota, T. Tsutsumi, and H. Kawarada, *J. Appl. Phys.* **77**, 1729 (1995).
- [38] H. Kawarada, H. Matsuyama, Y. Yokota, T. Sogi, A. Yamaguchi, and A. Hiraki, *Phys. Rev. B* **47**, 3633 (1993).
- [39] J. Barjon, T. Tillocher, N. Habka, O. Brinza, J. Achard, R. Issaoui, F. Silva, C. Mer, and P. Bergonzo, *Phys. Rev. B* **83**, 073201 (2011).
- [40] J. Barjon, *Phys. Status Solidi* **214**, 1700402 (2017).
- [41] J. Isoya, H. Kanda, and Y. Uchida, *Phys. Rev. B* **42**, 9843 (1990).
- [42] A. M. Zaitsev, *Optical Properties of Diamond* (Springer, Berlin, 2001).
- [43] A. T. Collins, H. Kanda, and R. C. Burns, *Philos. Mag. Part B* **61**, 797 (1990).
- [44] J. P. Goss, P. R. Briddon, R. Jones, and S. Oberg, *J. Phys.: Condens. Matter* **16**, 4567 (2004).
- [45] M. H. Nazare, A. J. Neves, and G. Davies, *Phys. Rev. B* **43**, 14196 (1991).
- [46] P. Johnson and E. Myagkaya, *Gems Gemol.* **53**, 96 (2017).
- [47] L. J. Rogers, K. D. Jahnke, M. W. Doherty, A. Dietrich, L. P. McGuinness, C. Müller, T. Teraji, H. Sumiya, J. Isoya, N. B. Manson, and F. Jelezko, *Phys. Rev. B* **89**, 235101 (2014).
- [48] M. Lesik, J.-P. P. Tetienne, A. Tallaire, J. Achard, V. Mille, A. Gicquel, J.-F. F. Roch, and V. Jacques, *Appl. Phys. Lett.* **104**, 113107 (2014).
- [49] E. Neu, M. Fischer, S. Gsell, M. Schreck, and C. Becher, *Phys. Rev. B* **84**, 205211 (2011).
- [50] K. Iakoubovskii and G. Davies, *Phys. Rev. B* **70**, 245206 (2004).
- [51] A. T. Collins, *J. Phys. Condens. Matter* **1**, 439 (1999).
- [52] H. Klapper, in *Handbook of Crystal Growth* (Springer, Berlin, 2010), pp. 93–132.
- [53] I. V. Klepikov, A. V. Koliadin, and E. A. Vasilev, *IOP Conf. Ser. Mater. Sci. Eng.* **286**, 012035 (2017).
- [54] R. C. Burns, J. O. Hansen, R. A. Spits, M. Sibanda, C. M. Welbourn, and D. L. Welch, *Diam. Relat. Mater.* **8**, 1433 (1999).
- [55] C. J. Stephen, B. L. Green, Y. N. D. Lekhai, L. Weng, P. Hill, S. Johnson, A. C. Frangeskou, P. L. Diggles, M. J. Strain, E. Gu, M. E. Newton, J. M. Smith, P. S. Salter, and G. W. Morley, *Phys. Rev. Appl.* **12**, 064005 (2019).
- [56] A. Yelisseyev, Y. Babich, V. Nadolinny, D. Fisher, and B. Feigelson, *Diam. Relat. Mater.* **11**, 22 (2002).
- [57] U. F. S. S. D'Haenens-Johansson, A. M. Edmonds, B. L. Green, M. E. Newton, G. Davies, P. M. Martineau, R. U. A. Khan, and D. J. Twitchen, *Phys. Rev. B* **84**, 245208 (2011).
- [58] K. Iakoubovskii, *Phys. Rev. B* **70**, 205211 (2004).
- [59] T. Miyazaki, Y. Miyamoto, T. Makino, H. Kato, S. Yamasaki, T. Fukui, Y. Doi, N. Tokuda, M. Hatano, and N. Mizuoichi, *Appl. Phys. Lett.* **105**, 261601 (2014).



- [60] K. Iakoubovskii and A. T. Collins, *J. Phys.: Condens. Matter* **16**, 6897 (2004).
- [61] M. W. Dale, *Colour Centres on Demand in Diamond* (University of Warwick, Coventry, UK, 2015).
- [62] H. Pinto, R. Jones, D. W. Palmer, J. P. Goss, P. R. Briddon, and S. Oberg, *Phys. Status Solidi A* **209**, 1765 (2012).
- [63] A. T. Collins, *J. Phys. C* **13**, 2641 (1980).
- [64] M. N. R. Ashfold, J. P. Goss, B. L. Green, P. W. May, M. E. Newton, and C. V. Peaker, *Chem. Rev.* **120**, 5745 (2020).
- [65] B. L. Green, M. W. Dale, M. E. Newton, and D. Fisher, *Phys. Rev. B* **92**, 165204 (2015).
- [66] A. R. Lang and G. M. Meaden, *J. Cryst. Growth* **108**, 53 (1991).
- [67] H. Sumiya, N. Toda, and S. Satoh, *J. Cryst. Growth* **237-239**, 1281 (2002).
- [68] V. V. Lysakovskii, *J. Superhard Mater.* **36**, 303 (2014).
- [69] Y. Guo, Y. Feng, and L. Zhang, *Diam. Relat. Mater.* **61**, 91 (2016).
- [70] A. M. Zaitsev, K. S. Moe, and W. Wang, *Diam. Relat. Mater.* **71**, 38 (2017).
- [71] See Supplemental Material at <http://link.aps.org/supplemental/10.1103/PhysRevMaterials.4.093402> for comparative results on a diamond sample grown by HPHT synthesis from a different supplier.